

A micromorphic phase-field model for brittle and quasi-brittle fracture

Ritukesh Bharali¹, Fredrik Larsson¹, and Ralf Jänicke²

¹*Department of Industrial and Material Science, Chalmers University of Technology*

²*Institute of Applied Mechanics, Technische Universität Braunschweig*

Highlights

- *First* micromorphic approach towards phase-field fracture modelling.
- Phase-field is transformed to a local quantity and micromorphic variable regularises the problem.
- Model admits point-wise (local) treatment of fracture irreversibility.
- System precision fracture irreversibility achieved.
- Dimension of the problem remains same as conventional phase-field models.
- Numerical experiments carried out on benchmark brittle and quasi-brittle fracture problems.

Abstract

The phase-field model for fracture, despite its popularity and ease of implementation comes with its set of computational challenges. They are the non-convex energy functional, variational inequality due to fracture irreversibility, the need for extremely fine meshes to resolve the fracture. In this manuscript, the focus is on the numerical treatment of variational inequality. In this context, the popular history-variable approach suffers from variationally inconsistency and non-quantifiable nature of the error introduced. A better alternative, the penalisation approach, has the potential to render the stiffness matrix ill-conditioned. In order to circumvent both aforementioned issues, a micromorphic approach towards phase-field fracture modelling is proposed in this manuscript. Within this approach, a micromorphic extension of the energy functional is carried out. This transforms the phase-field into a local variable, while introducing a micromorphic variable that regularises the fracture problem. This reduction the regularity requirements for the phase-field enables an easier implementation of the fracture irreversibility constraint through simple ‘max’ operation, with system level precision. Numerical experiments carried out on benchmark brittle and quasi-brittle problems demonstrate the applicability and efficacy of the proposed model for a wide range of fracture problems.

Keywords: phase-field fracture, brittle, quasi-brittle, micromorphic, monolithic, fracture irreversibility

1 Introduction

The phase-field (smeared) fracture model is a promising alternative to conventional discrete fracture modelling techniques like XFEM [1, 2], Cohesive Zone models [3–5]. Unlike the discrete fracture modelling techniques, the phase-field fracture model offers a straightforward handling of topologically complex (branching, kinking and merging of cracks) fractures based on energy minimization. Moreover, it also has the ability to operate on fixed meshes, thus circumventing the need for tedious re-meshing techniques. A comprehensive comparison between discrete and smeared fracture modelling techniques has been carried out in [6].

The phase-field fracture model emerged from the variational treatment of the Griffith fracture criterion in [7], and its numerical adaptation in [8, 9]. The model introduces an auxiliary scalar variable, the phase-field, which interpolates between intact and fully broken (fractured) material states. The phase-field fracture model was cast into a thermodynamically consistent fracture in [10]. Since then, the model has been extended towards ductile fracture [11, 12], anisotropic fracture [13, 14], hydraulic fracture [15, 16], desiccation cracking [17, 18], corrosion [19, 20], fracture in thin films [21], to cite a few applications. It is imperative to mention that in these applications, the phase-field component was confined to brittle fracture. In [22], a unified phase-field fracture model was developed, encompassing both brittle and quasi-brittle fractures. Since then, the model has been applied in the investigation of size effect of concrete [23], hydrogen assisted cracking [24], electro-mechanical fracture in piezo-electric solids [25], and fracture of thermo-elastic solids [26], to cite a few. Although, comparatively fewer compared to single-scale applications, the phase-field fracture model has been studied in the context of multi-scale techniques as well. The phase-field fracture model has been extended towards concurrent multi-scale modelling in [27–30] and hierarchical multi-scale modelling in [31, 32].

The popularity and ease of implementation of the phase-field fracture model, however, comes at the cost of its own set of computational challenges. These include (A) minimising a non-convex energy functional, (B) treatment of variational inequality due to the fracture irreversibility constraint, and (C) the need for extremely fine meshes to resolve the fracture zone. For a comprehensive review of these issues, the reader is referred to [33] and references therein. In this manuscript, the focus is solely on the numerical treatment of the fracture irreversibility constraint. In this context, [34, 35] opted for a simple penalisation technique, [36] proposed a primal-dual active set method, while [37, 38] adopted an Augmented Lagrangian formulation based on the Moreau-Yoshida indicator function. In an alternative approach, [39] introduced an implicit history-variable as the fracture driving energy in order to ensure fracture irreversibility. Among all techniques, the penalisation approach and the history-variable approach remain popular, owing to their ease in implementation into existing finite element frameworks. However, the penalisation approach has the potential to render a stiffness matrix ill-conditioned, particularly when a stricter irreversibility tolerance is desired. This is clear from the expressions for the penalty term derived in Section 3.3.3 in [35]. The history-variable circumvents the ill-conditioning of the stiffness matrix, however, it results in the loss of variational consistency of the problem. Furthermore, to the best of the authors’ knowledge, the error introduced with the history-variable approach is unknown. In order to circumvent potential ill-conditioning of stiffness matrix and non-quantifiable error, a micromorphic approach to phase-field fracture model is proposed in this manuscript.

The micromorphic approach for gradient elasticity, viscoplasticity and damage was proposed in [40]. Thereafter, the work has been extended towards crystal plasticity [41–43], small and finite deformation plasticity coupled with damage [44, 45] to cite a few. The micromorphic approach has been adopted in the context of ductile phase-field fracture in [46] for introducing a length-scale to the plastic zone. To the best of the authors’ knowledge, the micromorphic approach has not been explored in regard to brittle and quasi-brittle phase-field fracture models. This research gap is addressed in this manuscript, and subsequently, a simple way of enforcing the phase-field fracture irreversibility is demonstrated. To this end, the phase-field fracture energy functional is extended in the spirit of [40]. This transforms the phase-field into a local quantity, while introducing a ‘*new*’ micromorphic variable that regularises the problem. The local nature of the phase-field enables a simpler treatment¹ of the fracture irreversibility constraint, at material points (integration points). Furthermore, the dimension of the problem remains unchanged, with displacement and micromorphic variable being the nodal field quantities and the phase-field being a local material point variable.

¹in comparison to non-local quantities in the H^1 space

The efficacy of the novel micromorphic phase-field fracture model is demonstrated with benchmark problems in both brittle and quasi-brittle fracture. These include a single edge notched specimen under tension, the Winkler L-panel experiment [47], and a three-point bending experiment carried out in [48]. This manuscript is structured as follows: Section 2 introduces the reader to the phase-field model for fracture, its underlying energy functional and pertinent Euler-Lagrange equations. Subsequently, in Section 3, the micromorphic approach for phase-field fracture is introduced. The numerical benchmark problems are addressed in Section 4, followed by concluding remarks in Section 5.

2 Phase-field fracture model

2.1 The energy functional

Figure 1a and 1b illustrates a discrete fracture and a phase-field regularised fracture in a 2D continuum respectively. The salient feature of the a discrete fracture model is the explicit representation of the fracture through displacement discontinuities. The phase-field fracture model belongs to the smeared representation of fracture, where the phase-field, $\varphi \in [0, 1]$ interpolates between intact and fully broken (fractured) material states. The fractured continuum in both figures has to occupy a domain $\Omega \in \mathbb{R}^{\text{dim}}$ ($\text{dim} = 2$ in this case). The external boundary Γ comprises of the Dirichlet and Neumann boundaries, represented by Γ_D^u and Γ_N^u respectively. Note that $\Gamma = \Gamma_D^u \cup \Gamma_N^u$ and $\Gamma_D^u \cap \Gamma_N^u = \emptyset$.

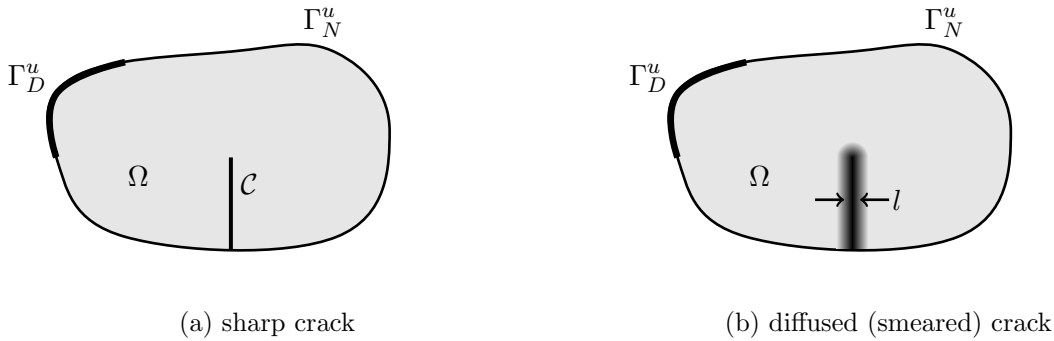


Figure 1: A solid $\Omega \in \mathbb{R}^2$ embedded with (a). sharp crack \mathcal{C} and (b). diffused (smeared) crack, with Dirichlet and Neumann boundaries indicated as Γ_D^u and Γ_N^u respectively. Figure adopted from [32]

The energy functional pertaining to the phase-field fracture model [33] is given by,

$$E(\mathbf{u}, \varphi) = \int_{\Omega} g(\varphi) \Psi^+(\boldsymbol{\epsilon}[\mathbf{u}]) \, d\Omega + \int_{\Omega} \Psi^-(\boldsymbol{\epsilon}[\mathbf{u}]) \, d\Omega - \int_{\Gamma_N^u} \mathbf{t}_p^u \cdot \mathbf{u} \, d\Gamma + \int_{\Omega} \frac{G_c}{c_w l} (w(\varphi) + l^2 |\nabla \varphi|^2) \, d\Omega, \quad (1)$$

where, a degradation function $g(\varphi)$ is attached to the fracture driving strain energy density Ψ^+ , with Ψ^- and \mathbf{t}_p^u being the residual strain energy density and the prescribed traction respectively. The last integral in the above equation represents the fracture energy, where G_c and l are the Griffith fracture energy and the fracture length-scale respectively, while c_w is a normalisation constant associated with the choice of the locally dissipated fracture energy function $w(\varphi)$. Some commonly adopted phase-field fracture models are presented in the Table 1.

The quasi-brittle phase-field fracture model requires additional parameters p , a_1 , a_2 and a_3 , as observed from the Table 1. These parameters are chosen in way, such that different traction-separation laws may be obtained. For a detailed derivation of these parameters, the reader is referred to [22]. Following [22], the constant a_1 is given by,

Fracture model	$w(\varphi)$	c_w	$g(\varphi)$
Brittle AT1 [49]	φ	8/3	$(1 - \varphi)^2$
Brittle AT2 [8]	φ^2	2	$(1 - \varphi)^2$
Quasi-brittle [22]	$2\varphi - \varphi^2$	π	$(1 - \varphi)^p$
			$(1 - \varphi)^p + a_1\varphi + a_1a_2\varphi^2 + a_1a_2a_3\varphi^3$

Table 1: Brittle and quasi-brittle phase-field fracture models.

$$a_1 = \frac{4E_0G_c}{\pi l f_t^2}, \quad (2)$$

where, the newly introduced parameters E_0 and f_t represent the Young's Modulus and the material tensile strength respectively. The other parameters vary for different traction-separation laws, and given in Table 2.

Traction-separation law	p	a_2	a_3
Linear Softening	2	-0.5	0
Exponential Softening	2.5	$2^{5/3} - 3$	0
Cornelissen et. al.[50] Softening	2	1.3868	0.6567

Table 2: Quasi-brittle phase-field fracture model parameters for different traction-separation laws [22].

As demonstrated in Equation (1), the strain energy density is split into fracture driving and residual components, Ψ^+ and Ψ^- . In this manuscript, the common consensus that a fracture occurs under tensile loading is adopted. Therefore, the fracture driving and residual strain energy densities are computed using the Amor split [49]. With this approach, the fracture is driven by the deviatoric part of the strain energy density together with a positive volumetric part of the strain energy density. The negative volumetric part corresponds to the residual energy. Mathematically,

$$\Psi^+ = \frac{1}{2}K \langle tr(\boldsymbol{\epsilon}) \rangle_+^2 + \mu(\boldsymbol{\epsilon}_{dev} : \boldsymbol{\epsilon}_{dev}) \quad (3)$$

and

$$\Psi^- = \frac{1}{2}K \langle tr(\boldsymbol{\epsilon}) \rangle_-^2. \quad (4)$$

Here, K and μ represents the bulk and the shear modulus of the material respectively, tr is a trace operator, $\langle \bullet \rangle_{\pm}$ represents the positive/negative Macaulay brackets, and $\boldsymbol{\epsilon}_{dev}$ is the deviatoric strain. The corresponding Cauchy stresses are given by,

$$\boldsymbol{\sigma}^+ := \frac{\partial \Psi^+}{\partial \boldsymbol{\epsilon}} = K \mathcal{H}(tr(\boldsymbol{\epsilon})) \mathbf{I} + 2\mu \boldsymbol{\epsilon}_{dev} \quad (5)$$

and

$$\boldsymbol{\sigma}^- := \frac{\partial \Psi^-}{\partial \boldsymbol{\epsilon}} = K \mathcal{H}(-tr(\boldsymbol{\epsilon})) \mathbf{I}, \quad (6)$$

adopting the heaviside function \mathcal{H} .

2.2 Euler-Lagrange equations

In order to simulate fracture initiation and propagation in continuum Ω , minimisation of the energy functional (1) is required, w.r.t. its solution variables \mathbf{u} and φ . This results in the Euler-Lagrange equations. Along with appropriately defined test and trial spaces, they result in the following problem:

Problem 1. Find $(\mathbf{u}, \varphi) \in \mathbb{U} \times \mathbb{P}$ with

$$\int_{\Omega} g(\varphi) \boldsymbol{\sigma}^+ : \boldsymbol{\epsilon}[\delta \mathbf{u}] \, d\Omega + \int_{\Omega} \boldsymbol{\sigma}^- : \boldsymbol{\epsilon}[\delta \mathbf{u}] \, d\Omega - \int_{\Gamma_N^{\mathbf{u}}} \mathbf{t}_p^u \delta \mathbf{u} \, d\Gamma = 0 \quad \forall \delta \mathbf{u} \in \mathbb{U}^0, \quad (7a)$$

$$\int_{\Omega} \frac{G_c}{c_w l} (w'(\varphi) (\hat{\varphi} - \varphi) + 2l^2 \nabla \varphi \cdot \nabla (\hat{\varphi} - \varphi)) \, d\Omega + \int_{\Omega} g'(\varphi) \Psi^+(\hat{\varphi} - \varphi) \, d\Omega \geq 0 \quad \forall \hat{\varphi} \in \mathbb{P}, \quad (7b)$$

using pertinent time-dependent Dirichlet boundary conditions \mathbf{u}^p on Γ_D^u and φ^p on Γ_D^φ , and Neumann boundary condition \mathbf{t}_p^u on Γ_N^u . The trial and test spaces are defined as

$$\mathbb{U} = \{\mathbf{u} \in [H^1(\Omega)]^{\dim} \mid \mathbf{u} = \mathbf{u}^p \text{ on } \Gamma_D^u\}, \quad (8a)$$

$$\mathbb{U}^0 = \{\mathbf{u} \in [H^1(\Omega)]^{\dim} \mid \mathbf{u} = \mathbf{0} \text{ on } \Gamma_D^u\}, \quad (8b)$$

$$\mathbb{P} = \{\varphi \in [H^1(\Omega)]^1 \mid \varphi \geq {}^n \varphi \mid \varphi = \varphi^p \text{ on } \Gamma_D^\varphi\}. \quad (8c)$$

Note that the requirement $\varphi \geq {}^n \varphi$ in (8c) ensures fracture irreversibility, with n referring to the previous time-step. ■

From Problem 1, it is clear that the fracture irreversibility constraint manifests in the form of a variationally inequality Euler-Lagrange equation (7b) with restrictive trial and test set (8c) for the phase-field. As mentioned in Section 1, several researchers have proposed different methods to treat the variational inequality problem. In the next section, a micromorphic phase-field fracture model is proposed, where the phase-field variable becomes a local quantity, while a micromorphic variable ensures regularisation of the problem. This enables a simpler ‘point-wise’ treatment of the fracture irreversibility constraint.

3 Micromorphic phase-field fracture model

3.1 Energy functional and variants

In this sub-section, a micromorphic extension of the phase-field fracture energy functional (1) is carried out in the spirit of [40]. This results in,

$$\begin{aligned} \tilde{E}(\mathbf{u}, \varphi, d) &= \int_{\Omega} g(\varphi) \Psi^+(\boldsymbol{\epsilon}[\mathbf{u}]) \, d\Omega + \int_{\Omega} \Psi^-(\boldsymbol{\epsilon}[\mathbf{u}]) \, d\Omega - \int_{\Gamma_N^u} \mathbf{t}_p^u \cdot \mathbf{u} \, d\Gamma \\ &+ \int_{\Omega} \frac{G_c}{c_w l} (w(\varphi) + l^2 |\nabla d|^2) \, d\Omega + \int_{\Omega} \frac{\alpha}{2} (\varphi - d)^2 \, d\Omega. \end{aligned} \quad (9)$$

Here, d is the ‘new’ micromorphic variable that regularises the fracture problem. From the above equation, it is observed that the micromorphic variable d is solely associated with the gradient term in the fracture energy integral, and the phase-field φ becomes a local quantity. Consequently, the regularity requirements on the phase-field w.r.t. the existence of derivatives is circumvented. Moreover, the micromorphic approach also introduces an *additional energy* term associated with the difference between the phase-field and the micromorphic variable. Theoretically, for the continuous problem, in the limit, the interaction parameter, $\alpha \rightarrow \infty$, the original energy functional (1) is recovered.

3.2 Euler-Lagrange equations

The set of Euler-Lagrange equations for the micromorphic phase-field fracture model is obtained upon minimising the energy functional (9) w.r.t. its solution variables \mathbf{u} , φ and d . Along with appropriately defined test and trial spaces, it results in the following problem:

Problem 2. Find $(\mathbf{u}, \varphi, d) \in \mathbb{U} \times \mathbb{P} \times \mathbb{D}$ with

$$\int_{\Omega} g(\varphi) \boldsymbol{\sigma}^+ : \boldsymbol{\epsilon}[\delta \mathbf{u}] \, d\Omega + \int_{\Omega} \boldsymbol{\sigma}^- : \boldsymbol{\epsilon}[\delta \mathbf{u}] \, d\Omega - \int_{\Gamma_N^{\mathbf{u}}} \mathbf{t}_p^{\mathbf{u}} \delta \mathbf{u} \, d\Gamma = 0 \quad \forall \delta \mathbf{u} \in \mathbb{U}^0, \quad (10a)$$

$$\int_{\Omega} g'(\varphi) \Psi^+(\hat{\varphi} - \varphi) \, d\Omega + \int_{\Omega} \frac{G_c}{c_w l} w'(\varphi) (\hat{\varphi} - \varphi) \, d\Omega + \int_{\Omega} \alpha(\varphi - d) (\hat{\varphi} - \varphi) \, d\Omega \geq 0 \quad \forall \hat{\varphi} \in \mathbb{P}, \quad (10b)$$

$$\int_{\Omega} \frac{2G_{cl}}{c_w} \nabla d \cdot \nabla \delta d \, d\Omega - \int_{\Omega} \alpha(\varphi - d) \delta d \, d\Omega = 0 \quad \forall \delta d \in \mathbb{D}, \quad (10c)$$

using pertinent time-dependent Dirichlet and Neumann boundary conditions, \mathbf{u}^p on $\Gamma_D^{\mathbf{u}}$, and $\mathbf{t}_p^{\mathbf{u}}$ on $\Gamma_N^{\mathbf{u}}$ respectively. The trial and test spaces are given by,

$$\mathbb{U} = \{\mathbf{u} \in [H^1(\Omega)]^{\dim} \mid \mathbf{u} = \mathbf{u}^p \text{ on } \Gamma_D^{\mathbf{u}}\}, \quad (11a)$$

$$\mathbb{U}^0 = \{\mathbf{u} \in [H^1(\Omega)]^{\dim} \mid \mathbf{u} = \mathbf{0} \text{ on } \Gamma_D^{\mathbf{u}}\}, \quad (11b)$$

$$\mathbb{D} = \{d \in [H^1(\Omega)]\}, \quad (11c)$$

$$\mathbb{P} = \{\varphi \in [L^2(\Omega)] \mid \varphi \geq {}^n \varphi\}. \quad (11d)$$

■

In Problem 2, the phase-field evolution equation (10b) is local. As such, φ can be computed ‘point-wise’ in the computational domain. In particular, the root(s) of the possibly nonlinear scalar equation,

$$g'(\varphi) \Psi^+(\boldsymbol{\epsilon}[\mathbf{u}]) + \frac{G_c}{c_w l} w'(\varphi) + \alpha(\varphi - d) = 0 \quad (12)$$

yield(s) the phase-field φ , if ${}^n \varphi < \varphi < 1$. Using the locally computed phase-field, the complete problem for micromorphic phase-field fracture is assumed the form:

Problem 3. Find $(\mathbf{u}, d) \in \mathbb{U} \times \mathbb{D}$ with

$$\int_{\Omega} g(\varphi) \boldsymbol{\sigma}^+ : \boldsymbol{\epsilon}[\delta \mathbf{u}] \, d\Omega + \int_{\Omega} \boldsymbol{\sigma}^- : \boldsymbol{\epsilon}[\delta \mathbf{u}] \, d\Omega - \int_{\Gamma_N^{\mathbf{u}}} \mathbf{t}_p^{\mathbf{u}} \delta \mathbf{u} \, d\Gamma = 0 \quad \forall \delta \mathbf{u} \in \mathbb{U}^0, \quad (13a)$$

$$\int_{\Omega} \frac{2G_{cl}}{c_w} \nabla d \cdot \nabla \delta d \, d\Omega - \int_{\Omega} \alpha(\varphi - d) \delta d \, d\Omega = 0 \quad \forall \delta d \in \mathbb{D}, \quad (13b)$$

using pertinent time-dependent Dirichlet boundary conditions \mathbf{u}^p on $\Gamma_D^{\mathbf{u}}$, and Neumann boundary condition $\mathbf{t}_p^{\mathbf{u}}$ on $\Gamma_N^{\mathbf{u}}$. The trial and test spaces are defined as

$$\mathbb{U} = \{\mathbf{u} \in [H^1(\Omega)]^{\dim} \mid \mathbf{u} = \mathbf{u}^p \text{ on } \Gamma_D^{\mathbf{u}}\}, \quad (14a)$$

$$\mathbb{U}^0 = \{\mathbf{u} \in [H^1(\Omega)]^{\dim} \mid \mathbf{u} = \mathbf{0} \text{ on } \Gamma_D^{\mathbf{u}}\}, \quad (14b)$$

$$\mathbb{D} = \{d \in [H^1(\Omega)]\}, \quad (14c)$$

with the local phase-field φ computed using (12). ■

It is worth mentioning that the local phase-field evolution (12) is linear for brittle AT1 and AT2 fracture models. This is due to the quadratic nature of the degradation function $g(\varphi) = (1 - \varphi)^2$ coupled with linear/quadratic locally dissipated fracture energy function $w(\varphi) = \varphi$ and φ^2 for the AT1 and AT2 models respectively. This yield explicit expressions for the local phase-field variable,

$$\varphi = \min \left(\max \left(\frac{2\Psi^+ + \alpha d - \frac{3G_c}{8l}}{2\Psi^+ + \alpha}, n\varphi \right), 1 \right), \quad (15)$$

for AT1, and

$$\varphi = \min \left(\max \left(\frac{2\Psi^+ + \alpha d}{2\Psi^+ + \alpha + \frac{G_c}{l}}, n\varphi \right), 1 \right). \quad (16)$$

for AT2 model respectively. In the case of quasi-brittle phase-field fracture model, the rational nature of the degradation function (see Table 1) results in nonlinear scalar equation for the local phase-field variable, warranting the need for the Newton-Raphson method.

3.3 Discrete equations

The work in this manuscript is executed within the framework of the finite element method [51, 52], using triangular (T3) elements for both, displacement and micromorphic fields. This allows assuming the displacement and the micromorphic fields at the nodes $(\tilde{\mathbf{u}}_i, \tilde{d}_i)$ as the primary unknowns, with the corresponding continuous fields (\mathbf{u}, d) approximated as,

$$\mathbf{u} = \sum_{i=1}^m N_i^{\mathbf{u}} \tilde{\mathbf{u}}_i, \quad d = \sum_{i=1}^m N_i^d \tilde{d}_i. \quad (17)$$

In the above equation, $N_i^{\mathbf{u}}$ and N_i^d are the interpolation functions for the displacement and the micromorphic phase-field, associated with the i^{th} node. The spatial derivatives of the interpolation functions $N_i^{\mathbf{u}}$ and N_i^d in a two-dimensional case are given by,

$$\mathbf{B}_i^{\mathbf{u}} = \begin{bmatrix} N_{i,x} & 0 \\ 0 & N_{i,y} \\ N_{i,y} & N_{i,x} \end{bmatrix}, \quad \mathbf{B}_i^d = \begin{bmatrix} N_{i,x} \\ N_{i,y} \end{bmatrix}. \quad (18)$$

Here, the subscripts $, x$ and $, y$ indicate spatial derivatives in x and y directions respectively. Using (18), the strain ϵ , and the gradient of the micromorphic variable ∇d are defined as,

$$\epsilon = \sum_{i=1}^m \mathbf{B}_i^{\mathbf{u}} \tilde{\mathbf{u}}_i, \quad \nabla d = \sum_{i=1}^m \mathbf{B}_i^d \tilde{d}_i. \quad (19)$$

The discrete phase-field fracture problem is obtained upon inserting (17-19) in the Euler-Lagrange equations from Problem 3. Thereafter, (13a) and (13b) are assumed as the internal forces, and stiffness matrix derived from its derivative. This notation is consistent with [53], and allows the presentation of the phase-field fracture problem in the incremental iterative framework as:

Discrete Problem 1. *Compute the solution increment $(\Delta \tilde{\mathbf{u}}, \Delta \tilde{d})_{i+1}$ in the current iteration $i + 1$ using*

$$\underbrace{\begin{bmatrix} \mathbf{K}^{\mathbf{u}\mathbf{u}} & \mathbf{K}^{\mathbf{u}d} \\ \mathbf{K}^{d\mathbf{u}} & \mathbf{K}^{dd} \end{bmatrix}}_{\text{Stiffness matrix}} \underbrace{\begin{Bmatrix} \Delta \tilde{\mathbf{u}} \\ \Delta \tilde{d} \end{Bmatrix}}_{i+1} = \underbrace{\begin{Bmatrix} \mathbf{f}^{\text{ext},\mathbf{u}} \\ \mathbf{f}^{\text{ext},d} \end{Bmatrix}}_i - \underbrace{\begin{Bmatrix} \mathbf{f}^{\text{int},\mathbf{u}} \\ \mathbf{f}^{\text{int},d} \end{Bmatrix}}_i, \quad (20a)$$

and update the solution fields,

$$\begin{Bmatrix} \tilde{\mathbf{u}} \\ \tilde{d} \end{Bmatrix}_{i+1} = \begin{Bmatrix} \tilde{\mathbf{u}} \\ \tilde{d} \end{Bmatrix}_i + \begin{Bmatrix} \Delta \tilde{\mathbf{u}} \\ \Delta \tilde{d} \end{Bmatrix}_{i+1}, \quad (20b)$$

until a certain convergence measure is fulfilled. The local element stiffness matrices are computed as:

$$\begin{aligned} \mathbf{K}^{uu} &= \int_{\Omega} [\mathbf{B}^u]^T \underbrace{\left(g(\varphi) \frac{\partial \boldsymbol{\sigma}^+}{\partial \boldsymbol{\epsilon}} + \frac{\partial \boldsymbol{\sigma}^-}{\partial \boldsymbol{\epsilon}} + g'(\varphi) \frac{\partial \varphi}{\partial \boldsymbol{\epsilon}} \boldsymbol{\sigma}^+ \right)}_{\mathbf{D}} [\mathbf{B}^u] d\Omega, \\ \mathbf{K}^{ud} &= \int_{\Omega} [\mathbf{B}^u]^T \left(g'(\varphi) \frac{\partial \varphi}{\partial d} \boldsymbol{\sigma}^+ \right) [N^d] d\Omega, \\ \mathbf{K}^{du} &= - \int_{\Omega} [N^d]^T \left(\alpha \frac{\partial \varphi}{\partial \boldsymbol{\epsilon}} \right) [\mathbf{B}^u] d\Omega, \\ \mathbf{K}^{dd} &= \int_{\Omega} \left\{ [\mathbf{B}^d]^T \left(\frac{2G_{cl}}{c_w} \right) [\mathbf{B}^d] + [N^d]^T \alpha \left(1 - \frac{\partial \varphi}{\partial d} \right) [N^d] \right\} d\Omega, \end{aligned} \quad (20c)$$

and the local internal force vectors are computed as

$$\begin{aligned} \mathbf{f}^{int,u} &= \int_{\Omega} [\mathbf{B}^u]^T (g(\varphi) \boldsymbol{\sigma}^+ + \boldsymbol{\sigma}^-) d\Omega, \\ \mathbf{f}^{int,d} &= \int_{\Omega} \left\{ [\mathbf{B}^d]^T \left(\frac{2G_{cl}}{c_w} \right) [\mathbf{B}^d] \tilde{d} - [N^d]^T \alpha (\varphi - d) \right\} d\Omega. \end{aligned} \quad (20d)$$

The external force vectors $\mathbf{f}^{int,u}$ and $\mathbf{f}^{int,d}$ are considered equal to zero. Computation of the material stiffness \mathbf{D} in Voigt notation is presented in Appendix A. \blacksquare

The discrete problem 1 is non-convex. As such, conventional incremental solution techniques, like the Newton-Raphson method fails to achieve convergence in the softening regime, possibly due to an indefinite stiffness matrix. Efforts to circumvent this issue include the novel line search technique proposed in [34], the use of arc-length solvers [54–56], trust-region methods [57] and convexification via extrapolation of the phase-field for the momentum balance equation [36]. These aforementioned techniques are within the framework of monolithic solution techniques. In [39], the alternate minimisation solution techniques was proposed, since the phase-field energy functional is convex with respect to either of the coupled field, if the other one is held constant. In this manuscript, a monolithic solution technique is desired. As such, the convexification strategy proposed by [36] is adopted. With this choice, the phase-field for the momentum balance equation $\hat{\varphi}$, is computed using,

$$g'(\hat{\varphi}) \Psi^+(\boldsymbol{\epsilon}[\mathbf{u}]) + \frac{G_c}{c_w l} w'(\hat{\varphi}) + \alpha(\hat{\varphi} - \hat{d}) = 0, \quad (21)$$

with \hat{d} being the linearly extrapolated micromorphic variable from the last two converged (time) steps. It is important to note that this extrapolation-based computation of the phase-field applies only to the momentum balance equation and not the micromorphic variable evolution equation. For the micromorphic variable evolution equation, the phase-field is computed using (12), restated below for clarity,

$$g'(\varphi) \Psi^+(\boldsymbol{\epsilon}[\mathbf{u}]) + \frac{G_c}{c_w l} w'(\varphi) + \alpha(\varphi - d) = 0. \quad (22)$$

Consequently, the discrete problem assumes the form:

Discrete Problem 2. Compute the solution increment $(\Delta \tilde{\mathbf{u}}, \Delta \tilde{d})_{i+1}$ in the current iteration $i + 1$ using

$$\underbrace{\begin{bmatrix} \mathbf{K}^{uu} & \mathbf{K}^{ud} \\ \mathbf{K}^{du} & \mathbf{K}^{dd} \end{bmatrix}}_{\text{Stiffness matrix}} \begin{Bmatrix} \Delta \tilde{\mathbf{u}} \\ \Delta \tilde{d} \end{Bmatrix}_{i+1} = \underbrace{\begin{Bmatrix} \mathbf{f}^{ext,u} \\ \mathbf{f}^{ext,d} \end{Bmatrix}_i - \begin{Bmatrix} \mathbf{f}^{int,u} \\ \mathbf{f}^{int,d} \end{Bmatrix}_i}_{\text{Residual}}, \quad (23a)$$

and update the solution fields,

$$\begin{Bmatrix} \tilde{\mathbf{u}} \\ \tilde{d} \end{Bmatrix}_{i+1} = \begin{Bmatrix} \tilde{\mathbf{u}} \\ \tilde{d} \end{Bmatrix}_i + \begin{Bmatrix} \Delta \tilde{\mathbf{u}} \\ \Delta \tilde{d} \end{Bmatrix}_{i+1}, \quad (23b)$$

until a certain convergence measure is fulfilled. The local element stiffness matrices are computed as:

$$\begin{aligned} \mathbf{K}^{uu} &= \int_{\Omega} [\mathbf{B}^u]^T \underbrace{\left(g(\hat{\varphi}) \frac{\partial \boldsymbol{\sigma}^+}{\partial \boldsymbol{\epsilon}} + \frac{\partial \boldsymbol{\sigma}^-}{\partial \boldsymbol{\epsilon}} \right)}_{\mathbf{D}} [\mathbf{B}^u] d\Omega, \\ \mathbf{K}^{ud} &= \mathbf{0}, \\ \mathbf{K}^{du} &= - \int_{\Omega} [N^d]^T \left(\alpha \frac{\partial \varphi}{\partial \boldsymbol{\epsilon}} \right) [\mathbf{B}^u] d\Omega, \\ \mathbf{K}^{dd} &= \int_{\Omega} \left\{ [\mathbf{B}^d]^T \left(\frac{2G_c l}{c_w} \right) [\mathbf{B}^d] + [N^d]^T \alpha \left(1 - \frac{\partial \varphi}{\partial d} \right) [N^d] \right\} d\Omega, \end{aligned} \quad (23c)$$

and the local internal force vectors are computed as

$$\begin{aligned} \mathbf{f}^{int,u} &= \int_{\Omega} [\mathbf{B}^u]^T (g(\hat{\varphi}) \boldsymbol{\sigma}^+ + \boldsymbol{\sigma}^-) d\Omega, \\ \mathbf{f}^{int,d} &= \int_{\Omega} \left\{ [\mathbf{B}^d]^T \left(\frac{2G_c l}{c_w} \right) [\mathbf{B}^d] \tilde{d} - [N^d]^T \alpha (\varphi - d) \right\} d\Omega. \end{aligned} \quad (23d)$$

The local phase-fields $\hat{\varphi}$ and φ are computed using (21) and (22) respectively. The external force vectors $\mathbf{f}^{int,u}$ and $\mathbf{f}^{int,d}$ are considered equal to zero. Computation of the material stiffness \mathbf{D} in Voigt notation is presented in Appendix A. ■

4 Numerical Study

In this section, numerical experiments are carried out on brittle and quasi-brittle phase-field fracture problems. The problems in brittle fracture include the single edge notched specimen under tension and shear, and the three-point bending test [39], whereas for quasi-brittle fracture, the Winkler concrete L-panel experiment [47] and the concrete three point bending experiment [48] are analysed. For each problem, the geometry, loading conditions as well as the additional model parameters are presented in the respective sub-sections. The phase-field fracture topology in the final step of the analysis, and the load-displacement curves are also shown therein.

All problems are solved in a fully coupled (monolithic) sense, adopting the Newton-Raphson method. The iterative procedure is terminated when an error measure defined as ratio of the norm of the residual in the current iteration to that of the first iteration is less than a certain tolerance, tol . In this manuscript, $tol = 1e - 3$. The linear problem within each iteration is solved using the GMRES solver, preconditioned with an incomplete LU preconditioner. Moreover, for all numerical experiments, the interaction parameter α is parametrised as

$$\alpha = \beta \frac{G_c}{l}, \quad (24)$$

with β being a user-defined non-dimensional scalar.

4.1 Single Edge Notched specimen under Tension (SENT)

The single edge notched specimen [39] has been studied extensively under tensile and shear loading in the phase-field fracture literature. The geometry consists of a unit square (in mm) embedded with a horizontal

notch, midway along height and equal to half of the edge length as shown in Figure 2. The notch is modelled explicitly in the finite element mesh. A quasi-static loading is applied at the top boundary in the form of prescribed displacement increment $\Delta u = 1e - 4[\text{mm}]$ for the first 55 steps, following which it is changed to $1e - 6[\text{mm}]$. The bottom boundary remains fixed. The additional model parameters are presented in Table 3.

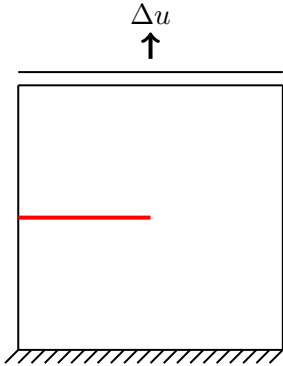


Figure 2: SENS experiment

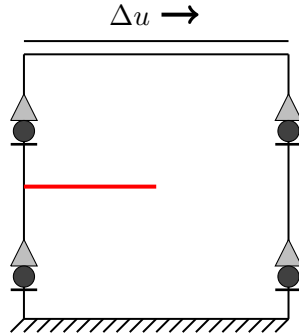


Figure 3: SENS experiment

Parameters	Value
Fracture Model	AT2
E_0	210.0 [GPa]
ν	0.3 [-]
G_c	2.7 [N/mm]
l	1.5e-2 [mm]
α	$\beta G_c / l$

Table 3: Model parameters

Figure 4a present the load-displacement curves, obtained using the micromorphic phase-field fracture model with different values of β . They are compared with the load-displacement curves from the literature [20, 39, 58]. While $\beta = 100, 250$ yield curves within the range of those from the literature, $\beta = 10$ predicts $\approx 24\%$ lower peak load. This is accompanied by a lower displacement at failure of the specimen, evident from the green curve in Figure 4a. In order to provide an explanation for this behaviour, both the phase-field and the micromorphic variable are plotted across the section, $x = 0.75$ [mm] in Figures 5a-5c, for varying β . For $\beta = 10$, the phase-field (φ) and the micromorphic variable (d) are not identical, indicating an insufficient interaction between the local and the non-local fields. Besides, comparing Figure 5a with Figures 5b and 5c, a second observation maybe made w.r.t. to the regularization. For $\beta = 10$, the phase-field values higher than 0.7 are not regularized. This results in local material response as the strength parameters (stress, stiffness) are dependant on the phase-field. This explains the different load-displacement response compared to those obtained from $\beta = 100, 250$. For the latter values, the phase-field fracture topology in the final step of the simulation in Figure 4b, is similar to those from the literature [20, 39, 58].

4.2 Single Edge Notched specimen under Shear (SENS)

In order to perform a shear test, the single edge notched specimen is loaded horizontally along the top edge as shown in Figure 3. The material properties remain same as presented in Table 3. A quasi-static loading is applied to the top boundary in the form of prescribed displacement increment $\Delta u = 1e - 4[\text{mm}]$ for the first 85 steps, following which it is changed to $5e - 6[\text{mm}]$. Furthermore, the bottom boundary remains fixed, and roller support is implemented in left and right edges thereby restricting the vertical displacement.

Figure 6a shows the load displacement curves obtained using $\beta = 10, 100, 250$. The curves obtained using $\beta = 100, 250$ is similar to that obtained in [59]. Moreover, the phase-field topology at the final step of the analysis (see Figure 6b) is similar to that presented in Figure 5 of [59]. For $\beta = 10$, the non-local behaviour of the micromorphic model is not sufficient. This explains the loss of integrity of specimen at an earlier stage in the loading process (cf. Figures 6a and 4a).

4.3 Winkler L-panel

The concrete L-shaped panel studied by [47, 60] is considered in this sub-section. Figure 7 shows the geometry as well as the loading conditions. The longer edges of the panel are 500 [mm] and the smaller edges are 250 [mm]. The loading is applied on the edge marked in blue, 30 [mm] in length, and is in the form of displacement increments of $\Delta u = 1e - 3$ [mm]. The additional model parameters are presented in Table 4.

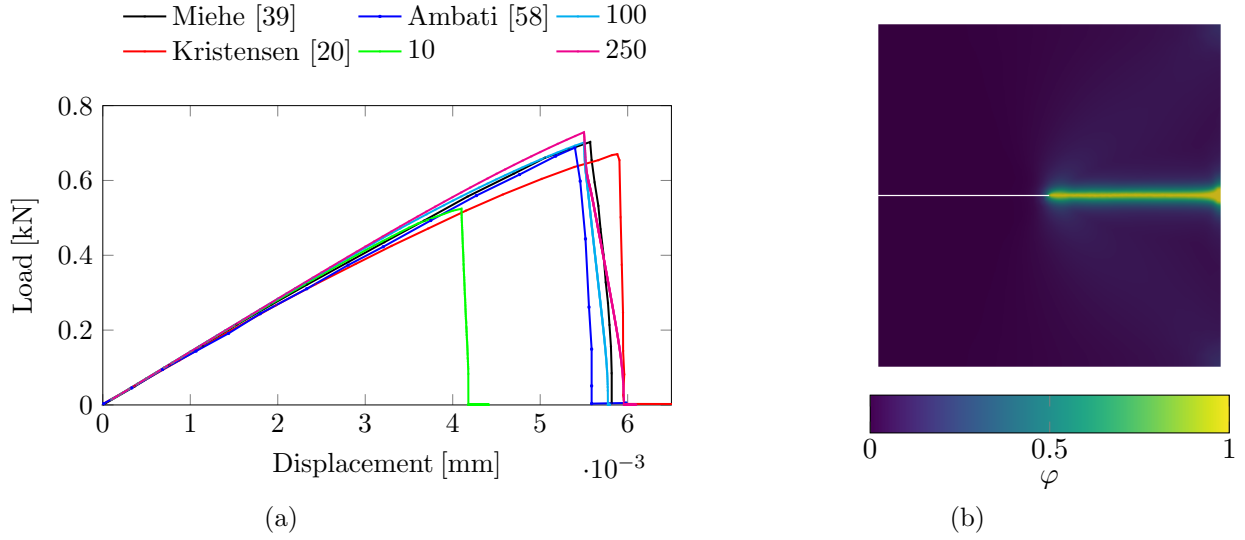


Figure 4: Figure (a) presents the load-displacement curves for the single edge notched specimen under tension. Here, β is varied as $\{10,100,250\}$. Figure (b) shows the distribution of the phase-field variable at the final step of the analysis.

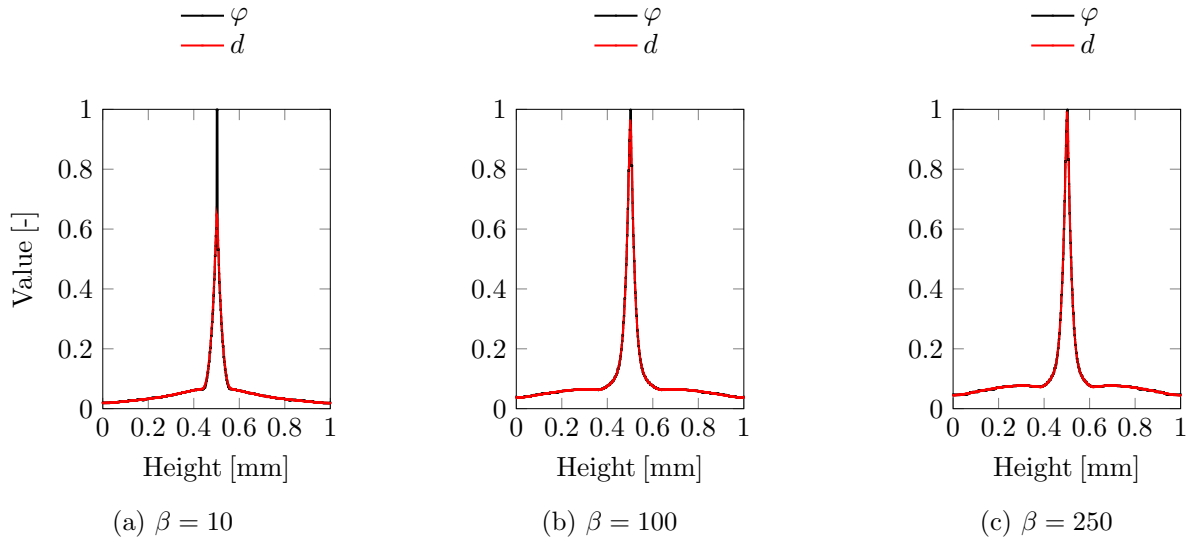


Figure 5: Figures present the phase-field (φ) and the micromorphic variable (d) for different β values at $x = 0.75$ [mm], along the height of the SENT specimen.

Figure 8a presents the load-displacement curves using the micromorphic phase-field fracture model, with $\beta = 100, 250$. The range of the experimentally obtained load-displacement curves is shown in the shaded region. For both values of β , the load-displacement curves exhibit a good agreement with the experimental region. Moreover, the phase-field topology in the final step of the simulation in Figure 8b is similar to that from the literature [47].

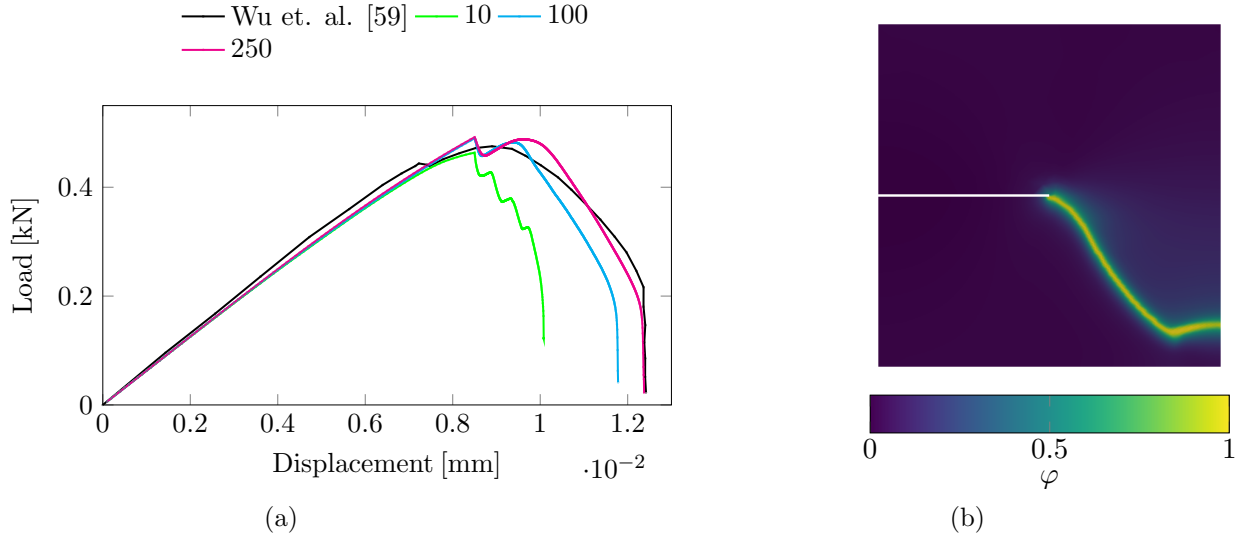


Figure 6: Figure (a) presents the load-displacement curves for the single edge notched specimen under shear. Here, β is varied as $\{100,250\}$. Figure (b) shows the distribution of the phase-field variable at the final step of the analysis.

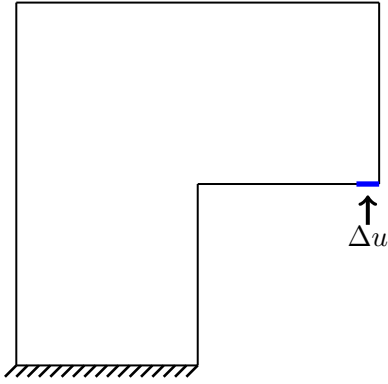


Figure 7: Winkler L-panel

Parameters	Value
Model	Quasi-brittle
Softening	Cornellisen et. al. [50]
E_0	$2.0e4$ [MPa]
ν	0.18 [-]
f_t	2.5 [MPa]
G_c	0.130 [N/mm]
l	10 [mm]
α	$\beta G_c/l$

Table 4: Parameters for L-shaped panel test [60]

4.4 Quasi-brittle: Concrete three-point bending

A three-point bending experiment on a notched concrete beam reported in [48] is considered here. The beam has dimensions 450×100 [mm²], and has a notch 5×50 [mm²]. A schematic of the beam along with the loading conditions is presented in Figure 9. Displacement-based load increments of $\Delta u = 1e - 3$ [mm] is enforced throughout the simulation. The model parameters are presented in Table 5.

Figure 10a presents the load-displacement curves using the micromorphic phase-field fracture model, with $\beta = 100, 250$. The range of the experimentally obtained load-displacement curves is exhibited by the shaded region. For both values of β , the load-displacement curves exhibit a good agreement with the experimental region. Moreover, the phase-field topology in the final step of the simulation in Figure 10b is similar to that from the literature [48].

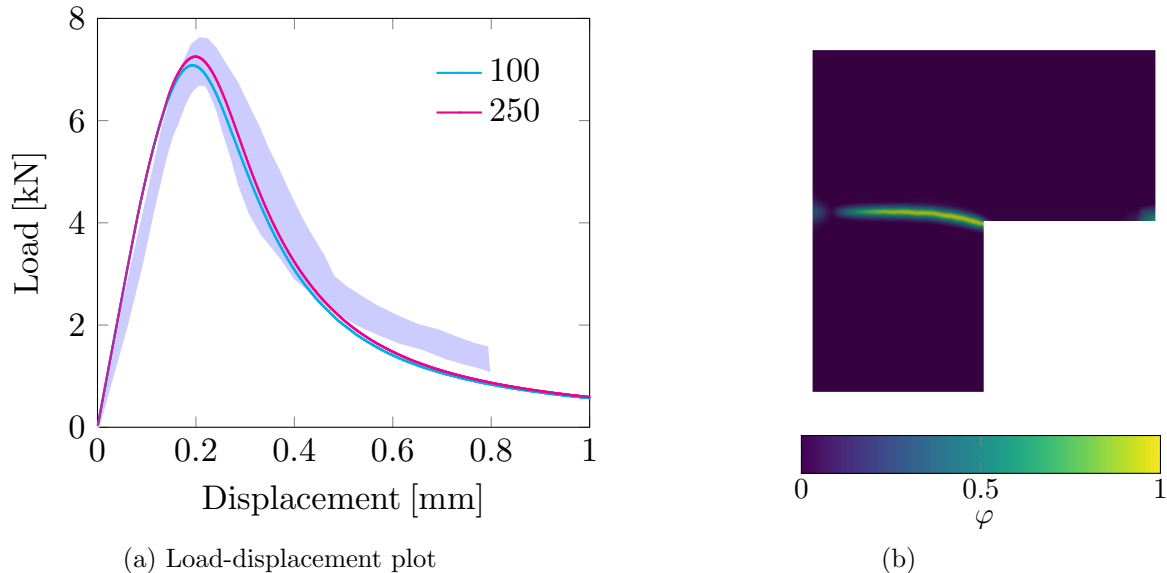


Figure 8: Figure (a) presents the load-displacement curves for the concrete Winkler L-panel test, for $\beta = 100, 250$. The experimental range is represented by the shaded area. Figure (b) shows the distribution of the phase-field variable at the final step of the analysis.

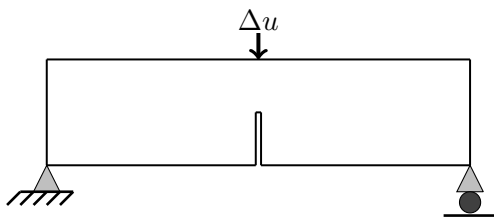


Figure 9: Three point bending test

Parameters	Value
Model	Quasi-brittle
Softening	Cornellisen et. al. [50]
E_0	2e4 [MPa]
ν	0.2 [-]
f_t	2.4 [MPa]
G_c	0.113 [N/mm]
l	2.5 [mm]
α	$\beta G_c/l$

Table 5: Parameters for three point bending test

5 Conclusions and Outlook

A novel phase-field fracture model is proposed in this manuscript, based on the micromorphic extension of the phase-field fracture energy functional. In this model, the phase-field variable is local, and a micromorphic variable is introduced for regularization. Combined with an irreversibility criterion on the phase-field variable, this results in a local variational inequality problem. The problem is then trivially solved pointwise (at integration points) throughout the computational domain. For brittle AT1 and AT2 models, an explicit expression for the local phase-field exists, however, for quasi-brittle fracture models, a nonlinear scalar equation needs to be solved. Furthermore, the local nature of the phase-field variable also provides the ease in implementing bounds, i.e., $\varphi \in [0, 1]$ using the trivial ‘*min*’ and ‘*max*’ operations. Unlike the penalization technique proposed in [35], fracture irreversibility is achieved with system precision without the need for a high penalty parameter. As regards to computational effort, since the phase-field variable is solved locally, the size of the finite element problem is identical to that of a standard phase-field implementation.

Furthermore, the micromorphic phase-field fracture model does converge towards the original phase-field model in the terms of the energy functional equivalence, when the interaction parameter α is chosen such

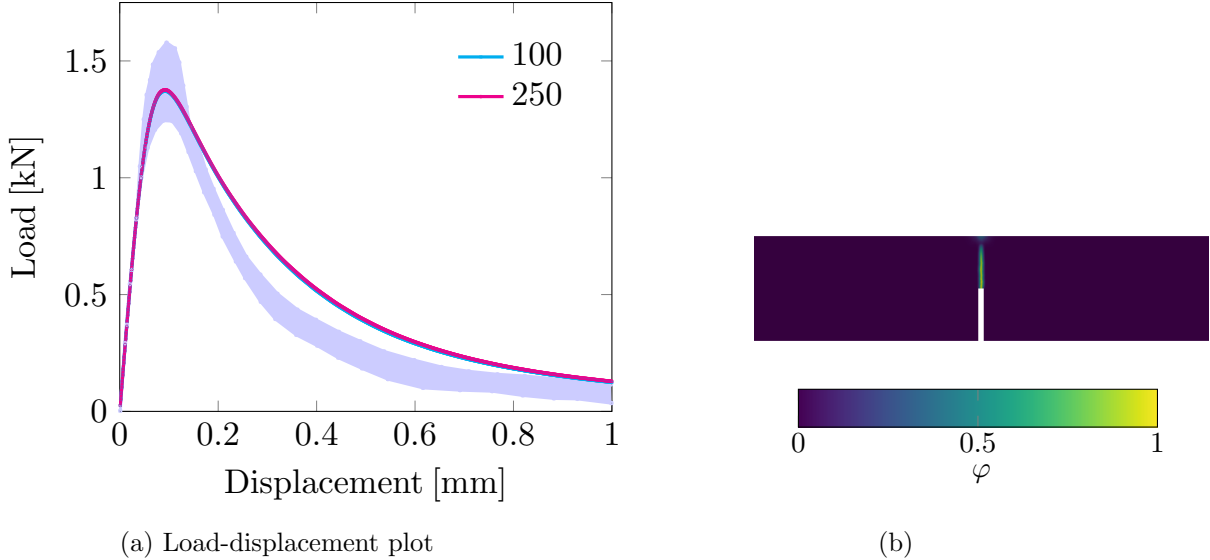


Figure 10: Figure (a) presents the load-displacement curves for the concrete three-point bending test, with $\beta = 100, 250$. The experimental range is represented by the shaded area. Figure (b) shows the distribution of the phase-field variable at the final step of the analysis in a section of the beam.

that $\varphi \approx d$. This has been demonstrated in this manuscript with numerical experiments on the single edge notched specimen loaded in tension. When the interaction parameter is sufficiently high ($\approx 250G_c/l$), the phase-field and the micromorphic variable profiles are similar for arbitrary sections in a computational domain. This essentially recovers the original phase-field fracture energy functional, while enabling the ease of local phase-field fracture irreversibility. Numerical experiments were also carried out in the context of quasi-brittle fracture, the Winkler L-shaped panel and the concrete three-point bending tests. It is observed that the micromorphic phase-field fracture model results in fracture topologies and load-displacement curves within the experimentally observed range. This demonstrates capability of the micromorphic approach to demonstrate both brittle and quasi-brittle phenomenon.

Finally, the novel micromorphic phase-field fracture model opens a plethora of future research extensions, particularly, in multi-physics applications, composite laminates [61]. Other studies may include the implementation of a dissipation-based arc-length method [55, 56] or quasi-Newton methods [62, 63] for addressing the non-convexity of energy functional.

6 Software Implementation and Data Availability

The numerical study in Section 5 is carried out using an in-house finite element code, inspired by ofeFrac [64], and based on the Jem and Jive C++ libraries from the Dynaflow Research Group, the Netherlands. The simulation data would be made available in Github repository of the corresponding author (<https://github.com/ritukeshbharali>).

Declaration of Competing Interest

The authors declare that they have no known competing financial interests or personal relationships that could have appeared to influence the work reported in this paper.

Acknowledgements

The financial support from the Swedish Research Council for Sustainable Development (FORMAS) under Grant 2018-01249 and the Swedish Research Council (VR) under Grant 2017-05192 is gratefully acknowledged. The first author would also like to thank Dr. Erik Jan Lingen at Dynaflo Research Group for support with the Jem and Jive libraries.

Appendix A Constitutive relation with Amor split [49]

In this manuscript, the fracture driving and residual strain energy densities are computed using the Amor split [49]. With this approach, the fracture is driven by the deviatoric part of the strain energy density together with a positive volumetric part of the strain energy density. The negative volumetric part corresponds to the residual energy. Adopting a Voigt notation, the constitutive material stiffness \mathbf{D} in (20c,23c),

$$\mathbf{D} = g(\hat{\varphi}) \frac{\partial \boldsymbol{\sigma}^+}{\partial \boldsymbol{\epsilon}} + \frac{\partial \boldsymbol{\sigma}^-}{\partial \boldsymbol{\epsilon}} \quad (\text{A.1})$$

is computed as,

$$\mathbf{D} = g(\hat{\varphi}) \left(K \mathcal{H}(\text{tr}(\boldsymbol{\epsilon})) \mathbb{P}_{vol} + 2\mu \mathbb{P}_{dev} \right) + K \mathcal{H}(-\text{tr}(\boldsymbol{\epsilon})) \mathbb{P}_{vol} \quad (\text{A.2})$$

with bulk and shear modulus K, μ , heaviside function \mathcal{H} and projection matrices,

$$\mathbb{P}_{vol} = \begin{bmatrix} 1 & 1 & 1 & 0 & 0 & 0 \\ 1 & 1 & 1 & 0 & 0 & 0 \\ 1 & 1 & 1 & 0 & 0 & 0 \\ 0 & 0 & 0 & 0 & 0 & 0 \\ 0 & 0 & 0 & 0 & 0 & 0 \\ 0 & 0 & 0 & 0 & 0 & 0 \end{bmatrix} \quad (\text{A.3})$$

and

$$\mathbb{P}_{dev} = \begin{bmatrix} 2/3 & -1/3 & 1/3 & 0 & 0 & 0 \\ 1/3 & 2/3 & 1/3 & 0 & 0 & 0 \\ 1/3 & 1/3 & 2/3 & 0 & 0 & 0 \\ 0 & 0 & 0 & 1/2 & 0 & 0 \\ 0 & 0 & 0 & 0 & 1/2 & 0 \\ 0 & 0 & 0 & 0 & 0 & 1/2 \end{bmatrix}. \quad (\text{A.4})$$

References

- [1] Natarajan Sukumar et al. “Extended finite element method for three-dimensional crack modelling”. In: *International journal for numerical methods in engineering* 48.11 (2000), pp. 1549–1570.
- [2] Nicolas Moës and Ted Belytschko. “Extended finite element method for cohesive crack growth”. In: *Engineering fracture mechanics* 69.7 (2002), pp. 813–833.
- [3] D.S. Dugdale. “Yielding of steel sheets containing slits”. In: *Journal of the Mechanics and Physics of Solids* 8.2 (1960), pp. 100–104. ISSN: 0022-5096. DOI: [https://doi.org/10.1016/0022-5096\(60\)90013-2](https://doi.org/10.1016/0022-5096(60)90013-2).

- [4] G.I. Barenblatt. “The Mathematical Theory of Equilibrium Cracks in Brittle Fracture”. In: ed. by H.L. Dryden et al. Vol. 7. *Advances in Applied Mechanics*. Elsevier, 1962, pp. 55–129. DOI: [https://doi.org/10.1016/S0065-2156\(08\)70121-2](https://doi.org/10.1016/S0065-2156(08)70121-2).
- [5] MGGV Elices et al. “The cohesive zone model: advantages, limitations and challenges”. In: *Engineering fracture mechanics* 69.2 (2002), pp. 137–163.
- [6] Adrian Egger et al. “Discrete and Phase Field Methods for Linear Elastic Fracture Mechanics: A Comparative Study and State-of-the-Art Review”. In: *Applied Sciences* 9.12 (2019). ISSN: 2076-3417. DOI: 10.3390/app9122436. URL: <https://www.mdpi.com/2076-3417/9/12/2436>.
- [7] G.A. Francfort and J.-J. Marigo. “Revisiting brittle fracture as an energy minimization problem”. In: *Journal of the Mechanics and Physics of Solids* 46.8 (Aug. 1998), pp. 1319–1342. ISSN: 00225096. DOI: 10.1016/S0022-5096(98)00034-9.
- [8] B. Bourdin, G.A. Francfort, and J.-J. Marigo. “Numerical experiments in revisited brittle fracture”. In: *Journal of the Mechanics and Physics of Solids* 48.4 (2000), pp. 797–826. ISSN: 0022-5096. DOI: [https://doi.org/10.1016/S0022-5096\(99\)00028-9](https://doi.org/10.1016/S0022-5096(99)00028-9).
- [9] B. Bourdin. “Numerical implementation of the variational formulation for quasi-static brittle fracture”. In: *Interfaces and Free Boundaries* 9 (2007), pp. 411–430. DOI: 10.4171/IFB/171.
- [10] Christian Miehe, Fabian Welschinger, and Martina Hofacker. “Thermodynamically consistent phase-field models of fracture: Variational principles and multi-field FE implementations”. In: *International journal for numerical methods in engineering* 83.10 (2010), pp. 1273–1311.
- [11] C. Miehe et al. “Phase field modeling of fracture in multi-physics problems. Part II. Coupled brittle-to-ductile failure criteria and crack propagation in thermo-elastic–plastic solids”. In: *Computer Methods in Applied Mechanics and Engineering* 294 (2015), pp. 486–522. ISSN: 0045-7825. DOI: <https://doi.org/10.1016/j.cma.2014.11.017>. URL: <https://www.sciencedirect.com/science/article/pii/S0045782514004435>.
- [12] M. Ambati, T. Gerasimov, and L. De Lorenzis. “Phase-field modeling of ductile fracture”. In: *Computational Mechanics* 55.5 (May 2015), pp. 1017–1040. ISSN: 1432-0924. DOI: 10.1007/s00466-015-1151-4. URL: <https://doi.org/10.1007/s00466-015-1151-4>.
- [13] S. Teichtmeister et al. “Phase field modeling of fracture in anisotropic brittle solids”. In: *International Journal of Non-Linear Mechanics* 97 (2017), pp. 1–21. ISSN: 0020-7462. DOI: <https://doi.org/10.1016/j.ijnonlinmec.2017.06.018>. URL: <https://www.sciencedirect.com/science/article/pii/S0020746217301944>.
- [14] Jeremy Bleyer and Roberto Alessi. “Phase-field modeling of anisotropic brittle fracture including several damage mechanisms”. In: *Computer Methods in Applied Mechanics and Engineering* 336 (2018), pp. 213–236. ISSN: 0045-7825. DOI: <https://doi.org/10.1016/j.cma.2018.03.012>. URL: <https://www.sciencedirect.com/science/article/pii/S0045782518301373>.
- [15] Zachary A. Wilson and Chad M. Landis. “Phase-field modeling of hydraulic fracture”. In: *Journal of the Mechanics and Physics of Solids* 96 (2016), pp. 264–290. ISSN: 0022-5096. DOI: <https://doi.org/10.1016/j.jmps.2016.07.019>. URL: <https://www.sciencedirect.com/science/article/pii/S002250961630285X>.

- [16] Y. Heider and B. Markert. “A phase-field modeling approach of hydraulic fracture in saturated porous media”. In: *Mechanics Research Communications* 80 (2017). Multi-Physics of Solids at Fracture, pp. 38–46. ISSN: 0093-6413. DOI: <https://doi.org/10.1016/j.mechrescom.2016.07.002>. URL: <https://www.sciencedirect.com/science/article/pii/S0093641316300714>.
- [17] Tuanny Cajuhi, Lorenzo Sanavia, and Laura De Lorenzis. “Phase-field modeling of fracture in variably saturated porous media”. In: *Computational Mechanics* 61.3 (2018), pp. 299–318.
- [18] Tianchen Hu, Johann Guilleminot, and John E. Dolbow. “A phase-field model of fracture with frictionless contact and random fracture properties: Application to thin-film fracture and soil desiccation”. In: *Computer Methods in Applied Mechanics and Engineering* 368 (2020), p. 113106. ISSN: 0045-7825. DOI: <https://doi.org/10.1016/j.cma.2020.113106>. URL: <https://www.sciencedirect.com/science/article/pii/S0045782520302905>.
- [19] Emilio Martínez-Pañeda, Alireza Golahmar, and Christian F. Niordson. “A phase field formulation for hydrogen assisted cracking”. In: *Computer Methods in Applied Mechanics and Engineering* 342 (2018), pp. 742–761. ISSN: 0045-7825. DOI: <https://doi.org/10.1016/j.cma.2018.07.021>. URL: <https://www.sciencedirect.com/science/article/pii/S0045782518303529>.
- [20] Philip K. Kristensen, Christian F. Niordson, and Emilio Martínez-Pañeda. “A phase field model for elastic-gradient-plastic solids undergoing hydrogen embrittlement”. In: *Journal of the Mechanics and Physics of Solids* 143 (2020), p. 104093. ISSN: 0022-5096. DOI: <https://doi.org/10.1016/j.jmps.2020.104093>. URL: <https://www.sciencedirect.com/science/article/pii/S0022509620303276>.
- [21] A. Mesgarnejad, B. Bourdin, and M.M. Khonsari. “A variational approach to the fracture of brittle thin films subject to out-of-plane loading”. In: *Journal of the Mechanics and Physics of Solids* 61.11 (2013), pp. 2360–2379. ISSN: 0022-5096. DOI: <https://doi.org/10.1016/j.jmps.2013.05.001>.
- [22] Jian-Ying Wu. “A unified phase-field theory for the mechanics of damage and quasi-brittle failure”. In: *Journal of the Mechanics and Physics of Solids* 103 (2017), pp. 72–99.
- [23] De-Cheng Feng and Jian-Ying Wu. “Phase-field regularized cohesive zone model (CZM) and size effect of concrete”. In: *Engineering Fracture Mechanics* 197 (2018), pp. 66–79. ISSN: 0013-7944. DOI: <https://doi.org/10.1016/j.engfracmech.2018.04.038>.
- [24] Jian-Ying Wu, Tushar Kanti Mandal, and Vinh Phu Nguyen. “A phase-field regularized cohesive zone model for hydrogen assisted cracking”. In: *Computer Methods in Applied Mechanics and Engineering* 358 (2020), p. 112614. ISSN: 0045-7825. DOI: <https://doi.org/10.1016/j.cma.2019.112614>.
- [25] Jian-Ying Wu and Wan-Xin Chen. “Phase-field modeling of electromechanical fracture in piezoelectric solids: Analytical results and numerical simulations”. In: *Computer Methods in Applied Mechanics and Engineering* 387 (2021), p. 114125. ISSN: 0045-7825. DOI: <https://doi.org/10.1016/j.cma.2021.114125>.
- [26] Tushar Kanti Mandal et al. “Fracture of thermo-elastic solids: Phase-field modeling and new results with an efficient monolithic solver”. In: *Computer Methods in Applied Mechanics and Engineering* 376 (2021), p. 113648. ISSN: 0045-7825. DOI: <https://doi.org/10.1016/j.cma.2020.113648>.

- [27] RU Patil, BK Mishra, and IV Singh. “A multiscale framework based on phase field method and XFEM to simulate fracture in highly heterogeneous materials”. In: *Theoretical and Applied Fracture Mechanics* 100 (2019), pp. 390–415.
- [28] Tymofiy Gerasimov et al. “A non-intrusive global/local approach applied to phase-field modeling of brittle fracture”. In: *Advanced modeling and simulation in engineering sciences* 5.1 (2018), pp. 1–30.
- [29] Lam H Nguyen and Dominik Schillinger. “The multiscale finite element method for nonlinear continuum localization problems at full fine-scale fidelity, illustrated through phase-field fracture and plasticity”. In: *Journal of Computational Physics* 396 (2019), pp. 129–160.
- [30] Savvas P Triantafyllou and Emmanouil G Kakouris. “A generalized phase field multiscale finite element method for brittle fracture”. In: *International Journal for Numerical Methods in Engineering* 121.9 (2020), pp. 1915–1945.
- [31] Bang He, Louis Schuler, and Pania Newell. “A numerical-homogenization based phase-field fracture modeling of linear elastic heterogeneous porous media”. In: *Computational Materials Science* 176 (2020), p. 109519.
- [32] Ritukesh Bharali, Fredrik Larsson, and Ralf Jänicke. “Computational homogenisation of phase-field fracture”. In: *European Journal of Mechanics - A/Solids* 88 (2021), p. 104247. ISSN: 0997-7538. DOI: <https://doi.org/10.1016/j.euromechsol.2021.104247>.
- [33] Laura De Lorenzis and Tymofiy Gerasimov. “Numerical implementation of phase-field models of brittle fracture”. In: *Modeling in Engineering Using Innovative Numerical Methods for Solids and Fluids*. Springer, 2020, pp. 75–101.
- [34] T. Gerasimov and L. De Lorenzis. “A line search assisted monolithic approach for phase-field computing of brittle fracture”. In: *Computer Methods in Applied Mechanics and Engineering* 312 (Dec. 2016), pp. 276–303. ISSN: 00457825. DOI: 10.1016/j.cma.2015.12.017.
- [35] Tymofiy Gerasimov and Laura De Lorenzis. “On penalization in variational phase-field models of brittle fracture”. In: *Computer Methods in Applied Mechanics and Engineering* 354 (2019), pp. 990–1026.
- [36] Timo Heister, Mary F. Wheeler, and Thomas Wick. “A primal-dual active set method and predictor-corrector mesh adaptivity for computing fracture propagation using a phase-field approach”. In: *Computer Methods in Applied Mechanics and Engineering* (2015). ISSN: 00457825. DOI: 10.1016/j.cma.2015.03.009.
- [37] Thomas Wick. “An Error-Oriented Newton/Inexact Augmented Lagrangian Approach for Fully Monolithic Phase-Field Fracture Propagation”. In: *SIAM Journal on Scientific Computing* 39.4 (2017), B589–B617. ISSN: 1064-8275. DOI: 10.1137/16m1063873.
- [38] Thomas Wick. “Modified Newton methods for solving fully monolithic phase-field quasi-static brittle fracture propagation”. In: *Computer Methods in Applied Mechanics and Engineering* 325 (2017), pp. 577–611. ISSN: 0045-7825. DOI: <https://doi.org/10.1016/j.cma.2017.07.026>.
- [39] Christian Miehe, Martina Hofacker, and Fabian Welschinger. “A phase field model for rate-independent crack propagation: Robust algorithmic implementation based on operator splits”. In: *Computer Methods in Applied Mechanics and Engineering* 199.45-48 (2010), pp. 2765–2778. ISSN: 00457825. DOI: 10.1016/j.cma.2010.04.011.

- [40] Samuel Forest. “Micromorphic approach for gradient elasticity, viscoplasticity, and damage”. In: *Journal of Engineering Mechanics* 135.3 (2009), pp. 117–131.
- [41] Samuel Forest et al. “Micromorphic approach to crystal plasticity and phase transformation”. In: *Plasticity and Beyond: Microstructures, Crystal-Plasticity and Phase Transitions*. Ed. by Jörg Schröder and Klaus Hackl. Vienna: Springer Vienna, 2014, pp. 131–198. ISBN: 978-3-7091-1625-8. DOI: 10.1007/978-3-7091-1625-8_3.
- [42] O. Aslan et al. “Micromorphic approach to single crystal plasticity and damage”. In: *International Journal of Engineering Science* 49.12 (2011). Advances in generalized continuum mechanics, pp. 1311–1325. ISSN: 0020-7225. DOI: <https://doi.org/10.1016/j.ijengsci.2011.03.008>.
- [43] Matti Lindroos et al. “Micromorphic crystal plasticity approach to damage regularization and size effects in martensitic steels”. In: *International Journal of Plasticity* 151 (2022), p. 103187. ISSN: 0749-6419. DOI: <https://doi.org/10.1016/j.ijplas.2021.103187>.
- [44] P. Grammenoudis, Ch. Tsakmakis, and D. Hofer. “Micromorphic continuum. Part III: Small deformation plasticity coupled with damage”. In: *International Journal of Non-Linear Mechanics* 45.2 (2010), pp. 140–148. ISSN: 0020-7462. DOI: <https://doi.org/10.1016/j.ijnonlinmec.2009.10.003>.
- [45] P. Grammenoudis, Ch. Tsakmakis, and D. Hofer. “Micromorphic continuum. Part II: Finite deformation plasticity coupled with damage”. In: *International Journal of Non-Linear Mechanics* 44.9 (2009), pp. 957–974. ISSN: 0020-7462. DOI: <https://doi.org/10.1016/j.ijnonlinmec.2009.05.004>.
- [46] C. Miehe, S. Teichtmeister, and F. Aldakheel. “Phase-field modelling of ductile fracture: a variational gradient-extended plasticity-damage theory and its micromorphic regularization”. In: *Philosophical Transactions of the Royal Society A: Mathematical, Physical and Engineering Sciences* 374.2066 (2016), p. 20150170. DOI: 10.1098/rsta.2015.0170.
- [47] Bernhard Josef Winkler. *Traglastuntersuchungen von unbewehrten und bewehrten Betonstrukturen auf der Grundlage eines objektiven Werkstoffgesetzes für Beton*. Innsbruck University Press, 2001.
- [48] Jan Rots. “Computational modeling of concrete fracture”. PhD thesis. Building 23, Stevinweg 1, 2628 CN, Delft, The Netherlands: Technische Universiteit Delft, 1988.
- [49] Kim Pham et al. “Gradient damage models and their use to approximate brittle fracture”. In: *International Journal of Damage Mechanics* 20.4 (2011), pp. 618–652.
- [50] H Cornelissen, D Hordijk, and H Reinhardt. “Experimental determination of crack softening characteristics of normalweight and lightweight”. In: *Heron* 31.2 (1986), pp. 45–46.
- [51] Olgierd Cecil Zienkiewicz et al. *The finite element method*. Vol. 3. McGraw-hill London, 1977.
- [52] Thomas JR Hughes. *The finite element method: linear static and dynamic finite element analysis*. Courier Corporation, 2012.
- [53] René De Borst et al. *Nonlinear finite element analysis of solids and structures*. John Wiley & Sons, 2012.
- [54] Julien Vignollet et al. “Phase-field models for brittle and cohesive fracture”. In: *Meccanica* 49.11 (2014), pp. 2587–2601.

- [55] Stefan May, Julien Vignollet, and Rene De Borst. “A numerical assessment of phase-field models for brittle and cohesive fracture: Γ -convergence and stress oscillations”. In: *European Journal of Mechanics-A/Solids* 52 (2015), pp. 72–84.
- [56] Ritukesh Bharali et al. “A robust monolithic solver for phase-field fracture integrated with fracture energy based arc-length method and under-relaxation”. In: *Computer Methods in Applied Mechanics and Engineering* 394 (2022), p. 114927. ISSN: 0045-7825. DOI: <https://doi.org/10.1016/j.cma.2022.114927>. URL: <https://www.sciencedirect.com/science/article/pii/S0045782522001992>.
- [57] Alena Kopaničáková and Rolf Krause. “A recursive multilevel trust region method with application to fully monolithic phase-field models of brittle fracture”. In: *Computer Methods in Applied Mechanics and Engineering* 360 (2020), p. 112720.
- [58] Marreddy Ambati, Tymofiy Gerasimov, and Laura De Lorenzis. “A review on phase-field models of brittle fracture and a new fast hybrid formulation”. In: *Computational Mechanics* 55.2 (Feb. 2015), pp. 383–405. ISSN: 1432-0924. DOI: 10.1007/s00466-014-1109-y.
- [59] Jian-Ying Wu et al. “Chapter One - Phase-field modeling of fracture”. In: ed. by Stéphane P.A. Bordas and Daniel S. Balint. Vol. 53. *Advances in Applied Mechanics*. Elsevier, 2020, pp. 1–183. DOI: <https://doi.org/10.1016/bs.aams.2019.08.001>. URL: <https://www.sciencedirect.com/science/article/pii/S0065215619300134>.
- [60] Jörg F Unger, Stefan Eckardt, and Carsten Könke. “Modelling of cohesive crack growth in concrete structures with the extended finite element method”. In: *Computer methods in applied mechanics and engineering* 196.41-44 (2007), pp. 4087–4100.
- [61] Tinh Quoc Bui and Xiaofei Hu. “A review of phase-field models, fundamentals and their applications to composite laminates”. In: *Engineering Fracture Mechanics* 248 (2021), p. 107705. ISSN: 0013-7944. DOI: <https://doi.org/10.1016/j.engfracmech.2021.107705>. URL: <https://www.sciencedirect.com/science/article/pii/S0013794421001582>.
- [62] Philip K. Kristensen and Emilio Martínez-Pañeda. “Phase field fracture modelling using quasi-Newton methods and a new adaptive step scheme”. In: *Theoretical and Applied Fracture Mechanics* 107 (2020), p. 102446. ISSN: 0167-8442. DOI: <https://doi.org/10.1016/j.tafmec.2019.102446>. URL: <https://www.sciencedirect.com/science/article/pii/S0167844219305580>.
- [63] Jian-Ying Wu, Yuli Huang, and Vinh Phu Nguyen. “On the BFGS monolithic algorithm for the unified phase field damage theory”. In: *Computer Methods in Applied Mechanics and Engineering* 360 (2020), p. 112704. ISSN: 0045-7825. DOI: <https://doi.org/10.1016/j.cma.2019.112704>. URL: <https://www.sciencedirect.com/science/article/pii/S0045782519305924>.
- [64] Chi Nguyen-Thanh et al. “Jive: An open source, research-oriented C++ library for solving partial differential equations”. In: *Advances in Engineering Software* 150 (2020), p. 102925. ISSN: 0965-9978. DOI: <https://doi.org/10.1016/j.advengsoft.2020.102925>.